Mercaptosilane-Assisted Synthesis of Metal Clusters within Zeolites and Catalytic Consequences of Encapsulation

Minkee Choi, Zhijie Wu, and Enrique Iglesia*

Department of Chemical Engineering, University of California at Berkeley, Berkeley, California 94720

Received April 4, 2010; E-mail: iglesia@berkeley.edu

Abstract: We report here a general synthetic strategy to encapsulate metal clusters within zeolites during their hydrothermal crystallization. Precursors to metal clusters are stabilized against their premature colloidal precipitation as hydroxides during zeolite crystallization using bifunctional (3-mercaptopropyl)trimethoxysilane ligands. Mercapto (−SH) groups in these ligands interact with cationic metal centers, while alkoxysilane moieties form covalent Si−O−Si or Si−O−Al linkages that promote zeolite nucleation around ligated metal precursors. These protocols led to the successful encapsulation of Pt, Pd, Ir, Rh, and Ag clusters within the NaA zeolite, for which small channel apertures (0.41 nm) preclude postsynthesis deposition of metal clusters. Sequential treatments in O_2 and H_2 formed small (∼1 nm) clusters with uniform diameter. Titration of exposed atoms with H_2 or O_2 gave metal dispersions that agree well with mean cluster sizes measured from electron microscopy and X-ray absorption spectroscopy, consistent with accessible cluster surfaces free of mercaptosilane residues. NaA micropore apertures restrict access to encapsulated clusters by reactants based on their molecular size. The ratio of the rates of hydrogenation of ethene and isobutene is much higher on clusters encapsulated within NaA than those dispersed on SiO_2, as also found for the relative rates of methanol and isobutanol oxidation. These data confirm the high encapsulation selectivity achieved by these synthetic protocols and the ability of NaA micropores to sieve reactants based on molecular size. Containment within small micropores also protects clusters against thermal sintering and prevents poisoning of active sites by organosulfur species, thus allowing alkene hydrogenation to persist even in the presence of thiophene. The bifunctional nature and remarkable specificity of the mercapto and alkoxysilane functions for metal and zeolite precursors, respectively, render these protocols extendable to diverse metal−zeolite systems useful as shape-selective catalysts in demanding chemical environments.
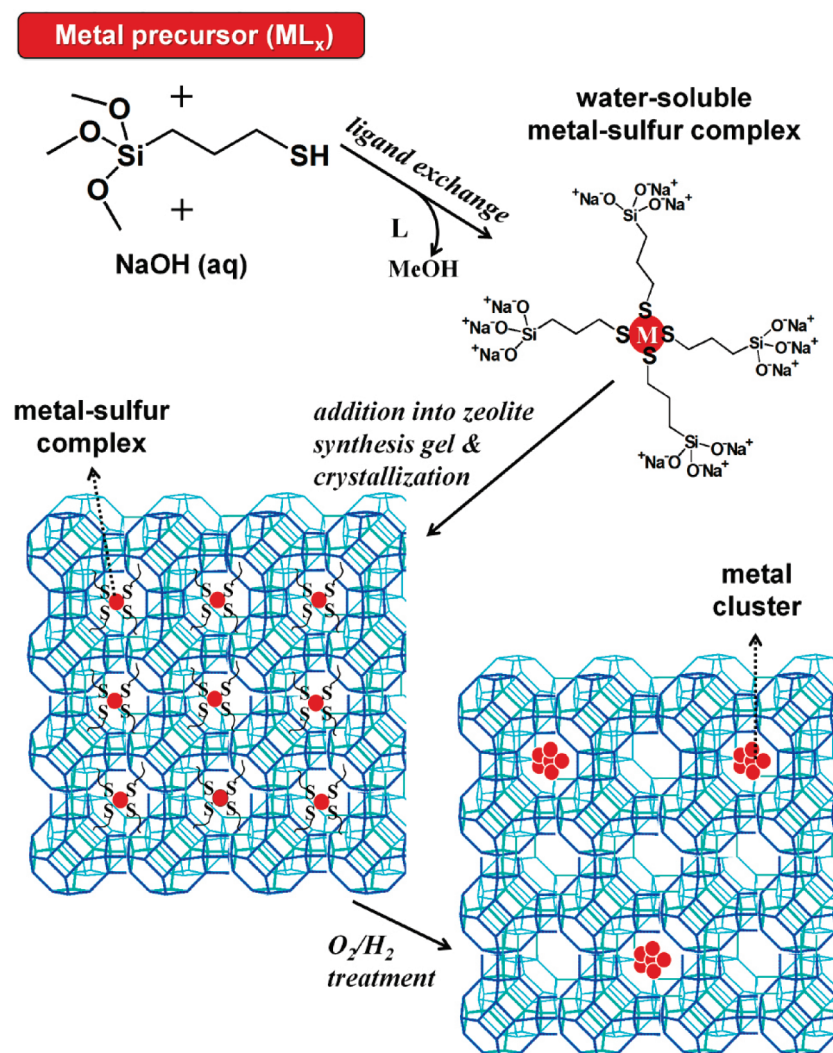
Introduction

The encapsulation of metal or metal oxide clusters within small voids in zeolites or other microporous solids can be used to contain and protect active structures and to select reactants, products, or transition states, thus providing diverse strategies for the design and synthesis of more effective catalysts.[1−3] The small and uniform size of channels and voids within crystalline microporous solids allows selective access of molecules to intracrystalline active sites based on size or shape. The placement of clusters within such constrained environments also tends to stabilize small clusters against sintering and poisoning more effectively than less restrictive mesoporous structures. Encapsulation within large-pore zeolites has been achieved by introducing metal precursors after zeolite crystallization using cation exchange,[1,2,4−9] impregnation,[2,10−12] or chemical vapor deposition.[2,13,14] These postsynthetic protocols are effective only for large-pore zeolites (12-member ring (MR) structures), such as FAU and MOR,[2,4−7,9−14] because smaller channels prevent access to intracrystalline spaces by solvated or gaseous precursors.[9] Ru[15] and Pt[16,17] clusters were recently encapsulated within small-pore zeolites (8-MR apertures) during hydrothermal zeolite synthesis; these clusters exhibited significant sulfur tolerance during hydrogenation reactions.[15,16] Small zeolite micropores restrict access to active sites by larger organosulfur species and allow H_2 dissociation on protected metal clusters to form hydrogen atoms that can be subsequently used to hydrogenate unsaturated molecules either directly[15] or on distant sites via spillover.[16−18]

(1) Sachtler, W. M. H. *Acc. Chem. Res.* **1993**, *26*, 383.
(2) Guczi, L.; Kiricsi, I. *Appl. Catal., A* **1999**, *186*, 375.
(3) Bein, T. *ACS Symp. Ser.* **1992**, *499*, 274.
(4) Ryoo, R.; Cho, S. J.; Pak, C.; Kim, J.-G.; Ihm, S.-K.; Lee, J. Y. *J. Am. Chem. Soc.* **1992**, *114*, 76.
(5) Ryoo, R.; Cho, S. J.; Pak, C. *Catal. Lett.* **1993**, *20*, 107.
(6) Cho, I. H.; Cho, S. J.; Park, S. B.; Ryoo, R. *J. Catal.* **1995**, *153*, 232.
(7) Sebastian, V.; Irusta, S.; Mallada, R.; Santamaría, J. *Appl. Catal. A: General* **2009**, *366*, 242.
(8) Li, X.; Iglesia, E. *Chem. Commun.* **2008**, 594.
(9) Djakovitch, L.; Koehler, K. *J. Am. Chem. Soc.* **2001**, *123*, 5990.
(10) Guzman, J.; Gates, B. C. *Dalton Trans.* **2003**, 3303.
(11) Uzun, A.; Gates, B. C. *Angew. Chem., Int. Ed.* **2008**, *47*, 9245.
(12) Fierro-Gonzalez, J. C.; Hao, Y.; Gates, B. C. *J. Phys. Chem. C* **2007**, *111*, 6645.
(13) Okamoto, Y.; Inui, Y.; Onimatsu, H.; Imanaka, T. *J. Phys. Chem.* **1991**, *95*, 4596.
(14) Abdo, S.; Howe, R. F. *J. Phys. Chem.* **1983**, *87*, 1713.
(15) Zhan, B.-Z.; Iglesia, E. *Angew. Chem., Int. Ed.* **2007**, *46*, 3697.
(16) Yang, H.; Chen, H.; Chen, J.; Omotoso, O.; Ring, Z. *J. Catal.* **2006**, *243*, 36.
(17) Chen, H.; Yang, H.; Omotoso, O.; Ding, L.; Briker, Y.; Zheng, Y.; Ring, Z. *Appl. Catal., A* **2009**, *358*, 103.
(18) Ohgoshi, S.; Nakamura, I.; Wakushima, Y. *Stud. Surf. Sci. Catal.* **1993**, *77*, 289.

Scheme 1. Schematic Representation of the Process for Mercaptosilane-Assisted Metal Encapsulation during Zeolite Crystallization

The direct encapsulation of metal precursors during hydrothermal synthesis[15–19] involves the introduction of solvated cationic complexes into an aluminosilicate gel and the assembly of zeolite building units around such species promoted by electrostatic or van der Waals interactions. The precipitation of precursors as bulk metal hydroxides cannot be generally synchronized with zeolite crystallization at the high pH required for the latter process; as a result, direct hydrothermal syntheses have not typically led to successful encapsulation using commonly used metal precursors. Many cationic precursors precipitate as bulk hydroxides in the alkaline media required for zeolite crystallization (Supporting Information, Figure S1), leading to the premature formation of colloidal particles too large for encapsulation. $RuCl_3$ and $Pt(NH_3)_4^{2+}$, however, can be encapsulated via direct methods because they do not form bulk hydroxides during hydrothermal synthesis. $Ru^{15,19}$ and $Pt^{16,17}$ clusters have been shown to form within small-pore LTA[15,16] and RHO,[17] and large-pore FAU[19] zeolites. We have recently found that Pd and Rh clusters can also be encapsulated

within LTA zeolite by chelating cations with protecting ethylene diamine ligands.[20]

Here, we report a general protecting strategy using bifunctional ligands ((3-mercaptopropyl)trimethoxysilane) that simultaneously stabilize the metal precursors against precipitation and promote the condensation of silicate structures around the ligated precursors (Scheme 1). The mercapto group (−SH) in these ligands binds strongly to late transition metals to form stable metal−sulfur adducts via ligand-exchange; they have been used to bind metal pollutants[21,22] and to prepare stable dispersions of colloidal metals.[23,24] These metal−sulfur adducts resist the formation of bulk metal hydroxides, even at the high pH required for zeolite synthesis. The alkoxysilane moiety of the mercaptosilane ligand undergoes hydrolysis in alkaline media to form covalent Si−O−Si or Si−O−Al bonds with nucleating zeolite structures, thus creating linkages that enforce encapsulation

(19) Zhan, B.-Z.; White, M. A.; Sham, T.-K.; Pincock, J. A.; Doucet, R. J.; Rao, K. V. R.; Robertson, K. N.; Cameron, T. S. *J. Am. Chem. Soc.* **2003**, *125*, 2195.

(20) Wu, Z.; Choi, M.; Iglesia, E. unpublished result.

(21) Celis, R.; Carmenhermosiän, M.; Cornejo, J. *Environ. Sci. Technol.* **2000**, *34*, 4593.

(22) Billinge, S. J. L.; McKimmy, E. J.; Shatnawi, M.; Kim, H. J.; Petkov, V.; Wermeille, D.; Pinnavaia, T. J. *J. Am. Chem. Soc.* **2005**, *127*, 8492.

(23) Brust, M.; Fink, J.; Bethell, D.; Schiffrin, D. J.; Kiely, C. *J. Chem. Soc., Chem. Commun.* **1995**, 1655.

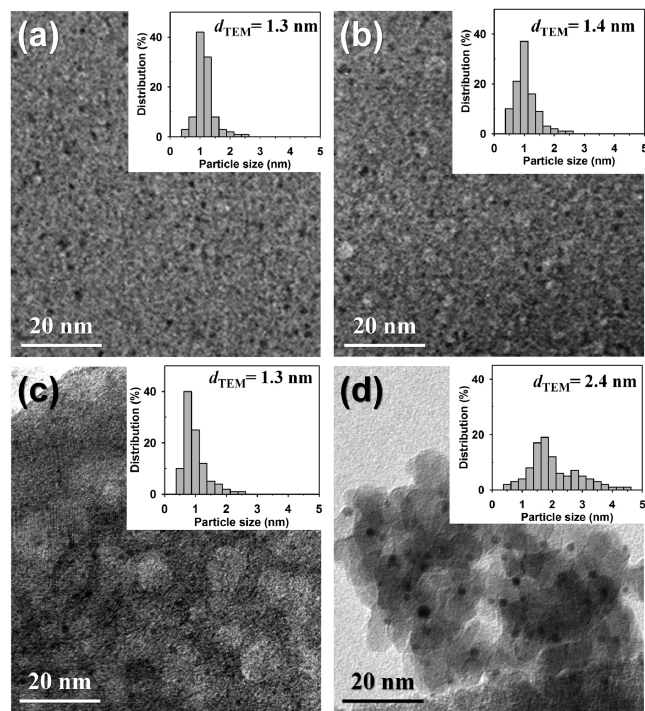(24) Zheng, N.; Stucky, G. D. *J. Am. Chem. Soc.* **2006**, *128*, 14278.

Figure 1. TEM images for (a) 1.1 wt % Pt/NaA, (b) 0.98 wt % Ir/NaA, (c) 1.0 wt % Rh/NaA samples synthesized by mercaptosilane-assisted hydrothermal crystallization, and (d) 0.79 wt % Pt/SiO$_2$ sample synthesized by a conventional impregnation method. Surface-area-weighted cluster diameters, d_{TEM}, were calculated from $d_{TEM} = \Sigma n_i d_i^3 / \Sigma n_i d_i^2$.[26,27]

Table 1. Metal Loading and Mean Diameter of Metal Clusters Dispersed in NaA and SiO$_2$

sample	metal loading (wt %)[a]	D[b]	d_{chem}[c] (nm)	d_{TEM}[d] (nm)
Pt/NaA	1.1[e] (0.07)[e]	0.92 (0.32)	1.2 (3.5)	1.3
Pt/SiO$_2$	0.79	0.61	1.9	2.4
Pd/NaA	1.0 (0.95)	0.65 (0.02)	1.7 (56)	1.9
Pd/SiO$_2$	0.55	0.38	2.9	3.1
Ir/NaA	0.98 (0.09)	0.69 (0.35)	1.5 (3.2)	1.4
Ir/SiO$_2$	1.1	0.74	1.3	1.4
Rh/NaA	1.0 (0.98)	0.83 (0.06)	1.3 (18)	1.3
Rh/SiO$_2$	1.1	0.60	1.8	2.1
Ag/NaA	0.97 (0.95)	0.99 (0.03)	1.2 (39)	1.3
Ag/SiO$_2$	1.0	0.26	4.5	4.7

[a] Analyzed by inductively coupled plasma optical emission spectroscopy. [b] Metal dispersion estimated from H$_2$ or O$_2$ chemisorption. [c] Mean cluster diameter estimated from metal dispersion and from $d_{chem} = C/D$, where C is 1.13, 1.12, 0.991, 1.10, and 1.18 nm for Pt, Pd, Ir, Rh, and Ag, respectively.[28,29] [d] Surface-area-weighted mean cluster diameter determined using TEM analysis and calculated from $d_{TEM} = \Sigma n_i d_i^3 / \Sigma n_i d_i^2$.[26,27] [e] The values outside brackets are for the NaA samples synthesized in the presence of mercaptosilane protecting ligand, while those inside brackets are for the NaA samples synthesized using the same condition but without mercaptosilane.

during subsequent zeolite crystal growth.[25] The dual function of this ligand causes the selective and quantitative encapsulation of most metals of catalytic interest (e.g., Pt, Pd, Ir, Rh, and Ag) during hydrothermal zeolite crystallization, as shown by the structural and functional characterization data reported here.

Results and Discussion

In the present work, we have directly crystallized NaA zeolite (LTA structure, 8-MR) containing Group VIIIB (Pt, Pd, Ir, Rh) and IB (Ag) metals in the presence of (3-mercaptopropyl)tri-methoxysilane (see the Experimental Section for the synthesis details). Inductively coupled plasma emission showed that >95% of the metal precursor in the synthesis mixture was incorporated into the final solid product. This remarkable selectivity reflects the strong and selective binding of the mercapto groups to the metal precursors and the preferential nucleation of the zeolite framework around these ligated metal precursors (via Si−O−Al or Si−O−Si bonds).

The protecting mercapto ligands were successfully removed by sequential treatments in O$_2$ and H$_2$ at 623 K (Ag was treated at 573 K). This process forms clusters that chemisorb H$_2$ and O$_2$ in amounts commensurate with the cluster size distributions evident from transmission electron micrographs (TEM). High-magnification TEM images (Figure 1 and Figure S2, Supporting Information) show that all visible metal clusters in NaA zeolite are uniform in diameter and distributed very narrowly around 1 nm. The surface-area-weighted cluster diameters, d_{TEM},[26,27]

were 1.3−1.9 nm for all the metal/NaA samples treated in O$_2$/H$_2$ (Table 1).

Chemisorptive titrations of metal surfaces with H$_2$ (Pt, Pd, Rh, and Ir) and O$_2$ (Ag) gives metal dispersions between 0.65 and 0.99 for all samples (Table 1). These dispersions correspond to mean cluster diameters (d_{chem}) of 1.2−1.7 nm, calculated by assuming spherical crystallites and the density of each bulk metal.[28,29] These cluster diameters are consistent with those measured by transmission electron microscopy (d_{TEM}) (Table 1). The excellent agreement between d_{chem} and d_{TEM} indicates that residues from the organosulfur protecting ligands can be completely removed from cluster surfaces by sequential O$_2$/H$_2$ treatments, and that cluster surfaces are fully accessible to H$_2$ and O$_2$ titrants, in spite of their location within the constrained environment of NaA cages.

The formation of spherical clusters similar in diameter to the NaA α-cage (1.1 nm) would correspond to metal dispersions of ∼0.90 for all metals[28,29] (∼50 atoms per cluster). Dispersions above 0.80 for Pt, Rh, and Ag/NaA catalysts reflect their essentially complete encapsulation within zeolite micropores. The slightly smaller dispersions measured for Pd (0.65) and Ir/NaA (0.68) samples may reflect the formation of a small number of larger metal clusters at zeolite external surfaces. Particle size distributions from TEM show that more than 90% of the clusters are smaller than 1.5 nm, even for Pd/NaA (Figure S2, Supporting Information) and Ir/NaA (Figure 1a). X-ray diffractograms (XRD) after O$_2$/H$_2$ treatment showed sharp lines indicative of crystalline NaA in all metal-containing samples, but no detectable lines corresponding to metal or oxide crystal structures (Figure S3, Supporting Information), consistent with the absence of bulk metal species and with the effective crystallization of NaA structures during ligand-assisted encapsulation protocols.

(25) Choi, M.; Cho, H. S.; Srivastava, R.; Venkatesan, C.; Choi, D.-H.; Ryoo, R. *Nat. Mater.* **2006**, *5*, 718.
(26) Schneider, M.; Duff, D. G.; Mallat, T.; Wildberger, M.; Baiker, A. *J. Catal.* **1994**, *147*, 500.
(27) Surface-area-weighted mean cluster diameter determined using TEM analysis and calculated from $d_{TEM} = \Sigma n_i d_i^3 / \Sigma n_i d_i^2$, where n_i is the number of crystallites having a diamerter d_i.
(28) Boudart, M.; Djega-Mariadassou, G. *The Kinetics of Heterogeneous Catalytic Reactions*, Princeton University Press, Princeton, NJ, 1984.
(29) Average particle diameter, d_{chem}, is obtained by $d_{chem} = f * V_{sp}/S_M$, where f is a shape factor, V_{sp} is the specific volume of the metal, and S_M is the specific surface area determined from chemisorption data. By assuming spherical geometry ($f = 6$) of metal clusters, d_{chem} is calculated by $d_{chem} = C/D$, where C is 1.13, 1.12, 0.991, 1.10 and 1.18 nm for Pt, Pd, Ir, Rh, and Ag, respectively.
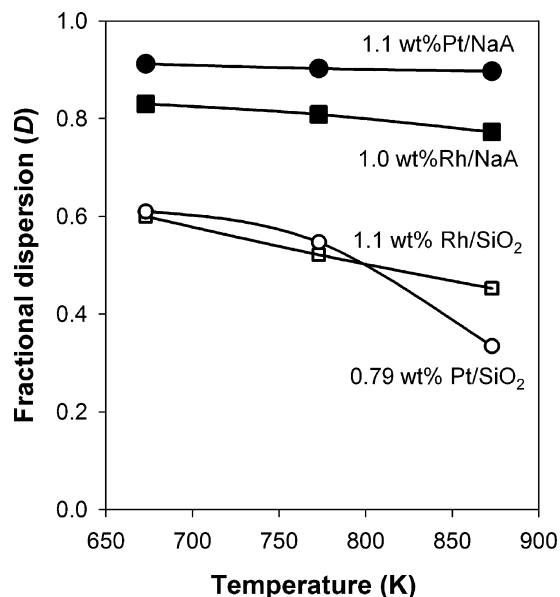
Figure 2. Effect of air treatment temperature on fractional metal dispersions (measured by H_2 chemisorption uptakes at 313 K) of Pt (circles) and Rh (squares) encapsulated within NaA zeolite (closed symbols) and supported on SiO_2 (open symbols). Samples were treated in flowing dry air (5 cm^3 g^{-1} s^{-1}) at the specified temperature for 6 h followed by treatment in flowing H_2 (5 cm^3 g^{-1} s^{-1}) at 623 K.

These data, taken together, indicate that all of these metals were encapsulated with very high selectivity within crystalline NaA α-cages during zeolite crystallization.

Metal/NaA samples generally showed much higher metal dispersions (0.65 − 0.99) than the corresponding metal/SiO_2 samples (0.26−0.74); the latter samples were prepared via impregnation with metal precursors to incipient wetness (Table 1). Clusters encapsulated within NaA microporous environments gave much narrower size distributions than those dispersed on SiO_2 (Figure 1). Similar effects of encapsulation within NaA α-cages are evident for the other metals (TEM images for Pd, Ir, Rh, and Ag on SiO_2 are shown in Figure S4, Supporting Information), indicating that the uniform microporous structure of NaA zeolite enables the formation of highly dispersed metal clusters with much greater size uniformity than on mesoporous supports.

Figure 2 shows the effects of thermal treatment in flowing dry air on metal dispersion for Pt and Rh clusters encapsulated within NaA and dispersed on SiO_2. The dispersions of Pt and Rh clusters in NaA zeolite decreased by less than 10% (0.91 to 0.90 for Pt, 0.83 to 0.77 for Rh) upon treatment in flowing dry air at 673−873 K and subsequent reduction in flowing H_2 at 623 K. In contrast, Pt and Rh clusters supported on SiO_2 showed a larger decrease in metal dispersion (25−46%) (0.61 to 0.33 for Pt, 0.60 to 0.45 for Rh) compared with those in NaA after similar treatments, in spite of the greater sintering stability expected of the larger clusters prevalent on SiO_2-supported samples. The higher stability of smaller clusters in NaA clearly shows that encapsulation within microporous environments protects metal clusters against sintering and coalescence during thermal treatments required in their synthesis and their regeneration during catalytic use.

We note that the use of the same metal precursors without the use of (3-mercaptopropyl)trimethoxysilane ligands during hydrothermal NaA synthesis gave very low metal dispersions or metal loadings (Table 1) because of segregated precipitation

of metal hydroxides (Figure S1, Supporting Information) or formation of anionic species, respectively. Low-magnification TEM images indicated that the absence of protecting mercaptosilane ligands in these synthetic protocol leads to physical mixtures of large Pd crystallites (>20 nm) and NaA crystals in Pd/NaA (Figure S5, Supporting Information). In this sample, sharp XRD peaks corresponding to metallic Pd were detected in addition to the peaks for NaA zeolite (Figure S5, Supporting Information). Selective encapsulation of Pt in NaA was achieved using a stable cationic $Pt(NH_3)_4^{2+}$ precursor[16,17] previously, but not with anionic H_2PtCl_6 species. The use of H_2PtCl_6 led to extremely low metal loading (0.07 wt %, Table 1). This can be attributed to the anionic nature of the precursor, which results in the lack of interaction between the metal species and the zeolite framework. Both cationic and anionic precursors, however, led to the successful encapsulation of Pt clusters upon ligation by bifunctional mercaptosilane ligands, because of the strong and preferential interactions of the mercapto group with the Pt centers in both precursors. Thus, we conclude that the method reported here allows successful metal encapsulation with a much more diverse range of metal precursors and without the need to synchronize colloidal hydroxide precipitation of precursors with the nucleation of the zeolite framework.

The structure and the chemical state of Pt were determined by X-ray absorption fine structure (XAFS) spectroscopy at various stages during the synthesis of Pt/NaA using mercaptosilanes as ligands. The resonant feature above the Pt L_{III} edge (Pt white line) was stronger for as-synthesized Pt/NaA sample than for bulk Pt metal or Pt/NaA samples after sequential O_2/H_2 treatments (Figure 3a), indicating the presence of Pt cations[30] upon encapsulation. Figure 3b shows the k^3-weighed radial structure functions obtained from the fine structure in the X-ray absorption spectrum of these samples (EXAFS). As-synthesized Pt/NaA gave a feature at 2.31 ± 0.01 Å, corresponding to Pt−S distances[31] but without detectable features for Pt−Pt coordination. The Pt−S coordination number (CN) was estimated to be 4.1 ± 0.6, consistent with square planar PtS_4−ligand complexes. Based on these XANES and EXAFS data, we conclude Pt(II)-S_4 complexes formed via reactions of mercaptosilanes with $PtCl_6^{2-}$, consistent with the observed formation of square-planar Pt(II)−S_4 complexes in the reactions of 3,5-ditert-butylbenzene-1,2-dithiolate with $PtCl_6^{2-}$.[32] The silane moieties in the protecting ligands act as nucleation points for the aluminolicate LTA framework. As a result, the extraframework $Pt(S−C_3H_7)_4$ is ~1.1 nm in its diagonal dimension, consistent with its encapsulation within α-cages in Na−LTA (1.1 nm diameter). The flexibility of its C−C and C−S bonds and of the framework lattice allows these species to reside within nucleating zeolite crystals during hydrothermal synthesis.

Subsequent thermal treatment in O_2 and H_2 at 623 K led to the predominant presence of Pt−Pt features (2.72 ± 0.01 Å) in the fine structure and to the disappearance of all Pt−S features, consistent with the full reduction of cationic precursors and with the substantial removal of sulfur heteratoms from Pt centers. The Pt−Pt coordination number measured from the fine structure was 6.6 ± 1.2; this value is consistent with the presence of

(30) Lytle, F. W.; Wei, P. S. P.; Greegor, R. B.; Via, G. H.; Sinfelt, J. H. *J. Chem. Phys.* **1979**, *70*, 4849.
(31) Huertas, S.; Hissler, M.; McGarrah, J. E.; Lachicotte, R. J.; Eisenberg, R. *Inorg. Chem.* **2001**, *40*, 1183.
(32) Ray, K.; Weyhermüller, T.; Neese, F.; Wieghardt, K. *Inorg. Chem.* **2005**, *44*, 5345.
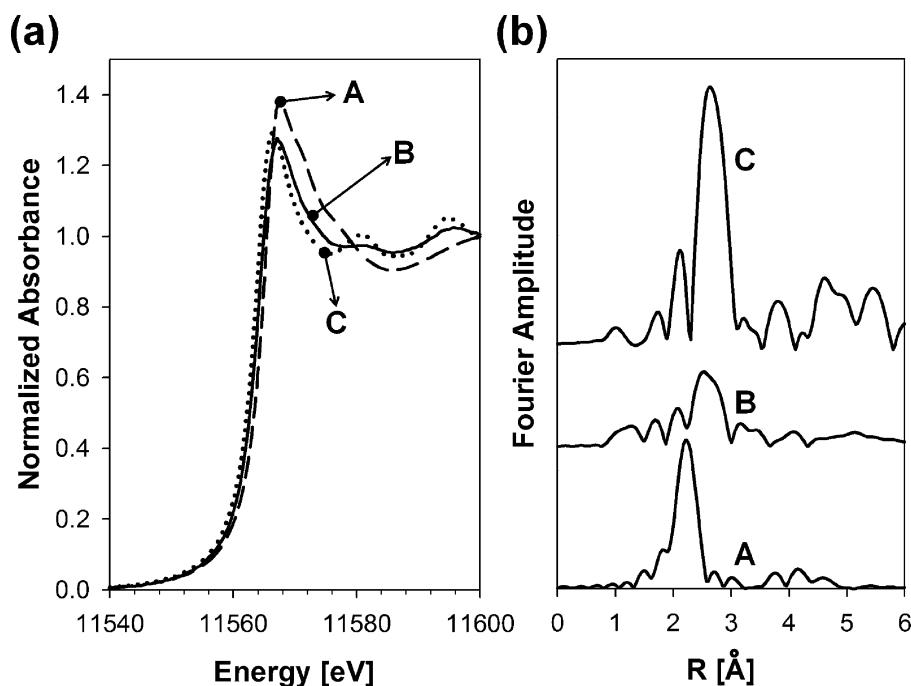
Figure 3. (a) X-ray absorption near edge structure (XANES) and (b) Fourier transforms of the k^3-weighted extended X-ray absorption fine structure (EXAFS) for 1.1 wt % of Pt/NaA samples at various stages in the mercaptosilane-assisted synthesis process (A, as-synthesized Pt/NaA; B, Pt/NaA treated in O_2 and H_2 at 623 K; C, bulk Pt).

Table 2. Catalytic Properties of Metal-Encapsulated NaA and Metal/SiO$_2$ Catalysts in Hydrogenation (HD) of Alkenes and Oxidative Dehydrogenation (ODH) of Alkanols[a]

sample	alkene hydrogenation turnover rates (mol · surf. g-atom^{-1} s^{-1})				alkanol oxidative dehydrogenation turnover rates (mol · surf. g-atom^{-1} s^{-1})			
	R_{ethene}[b]	$R_{isobutene}$[b]	χ_{HD}[c]	ϕ_{HD}[d]	$R_{methanol}$[b]	$R_{isobutanol}$[b]	χ_{ODH}[c]	ϕ_{ODH}[d]
Pt/NaA	0.57	0.0021	271	130	0.38	0.010	38	24
Pt/SiO$_2$	1.3	0.61	2.1		0.56	0.35	1.6	
Pd/NaA	0.59	0.013	47	9.8	0.11	0.018	5.7	2.6
Pd/SiO$_2$	1.6	0.34	4.8		0.51	0.23	2.2	
Ir/NaA	0.27	0.0030	90	100	0.092	0.011	8.1	6.2
Ir/SiO$_2$	0.70	0.80	0.88		0.19	0.15	1.3	
Rh/NaA	0.29	0.0070	42	75	0.013	0.0015	8.6	7.2
Rh/SiO$_2$	0.47	0.84	0.56		0.049	0.042	1.2	
Ag/NaA					0.043	0.0021	21	25
Ag/SiO$_2$					0.029	0.035	0.83	

[a] Hydrogenation: 1.5 kPa of alkene, 5 kPa of H$_2$, and 93.5 kPa of He at 294 K (except 373 K for Ir). Oxidative dehydrogenation: 4 kPa of alkanol, 9 kPa of O$_2$, and 87 kPa of He at 393 K (except 353 K for Pt). [b] Reaction turnover rate defined as molecules of reactant converted per time normalized by the number of exposed metal atoms derived from chemisorption uptakes. All the rates were determined at the reaction conversion less than 10%. [c] $\chi_{HD} = R_{ethene}/R_{isobutene}$, $\chi_{ODH} = R_{methanol}/R_{isobutanol}$. [d] Relative ratio of χ values for NaA and SiO$_2$ samples.

spherical clusters with 1.0 ± 0.2 nm diameters[33] in this sample. These diameters are similar to those of the α-cages in NaA (1.1 nm) and consistent with mean cluster diameters estimated from chemisorption uptakes and electron microscopy (Table 1). These data indicate that Pt−S bonds persist during hydrothermal synthesis and that metal clusters formed via sequential treatments in O$_2$ and H$_2$ are about 1 nm in diameter and do not retain detectable Pt−S coordination.

The ultimate arbiter of the successful encapsulation of these metal clusters is the demonstration of the intended benefits of constrained environments in their catalytic function, specifically in the ability of these materials to select reactants and transition states based on molecular size. We use here the relative turnover rates for hydrogenation (HD) of alkenes with different kinetic

diameter (ethene: 0.39 nm[34] and isobutene: 0.50 nm[35]) and for oxidative dehydrogenation (ODH) of alkanols with different kinetic diameter (methanol, 0.37 nm;[36] and isobutanol, 0.55 nm[36]). The specificity of encapsulation is then demonstrated by the ratio of turnover rates for small and large reactants on clusters dispersed within NaA and on SiO$_2$ samples (Table 2). The small windows in NaA (0.41 nm) allow essentially unrestricted access to encapsulated structures by ethene (kinetic diameter: 0.39 nm[34]) and methanol (0.37 nm[36]), but not by the larger isobutene (0.50 nm[35]) or isobutanol (0.55 nm[36]) reactants. As a result, the ratio of these turnover rates for small and large substrates (χ; Table 2) is much larger for clusters encapsulated

(33) Ramallo-López, J. M.; Requejo, F. G.; Craievich, A. F.; Wei, J.; Avalos-Borja, M.; Iglesia, E. *J. Mol. Catal. A* **2005**, *228*, 299.

(34) Triebe, R. W.; Tezel, F. H.; Khulbe, K. C. *Gas. Sep. Purif.* **1996**, *10*, 81.

(35) Boucheffa, Y.; Thomazeau, C.; Cartraud, P.; Magnoux, P.; Guisnet, M. *Ind. Eng. Chem. Res.* **1997**, *36*, 3198.

(36) Zhu, G.; Li, Y.; Zhou, H.; Liu, J.; Yang, W. *Mater. Lett.* **2008**, *62*, 4357.

Table 3. Selectivities in Methanol Oxidative Dehydrogenation[a]

catalyst	conv (%)	selectivity[b] (%)			
		HCHO	MF	DMM	CO_2
Pt/NaA	1.7	91.0	3.4	0.6	4.6
Pt/SiO$_2$	2.4	84.0	7.5	1.4	6.8
Pd/NaA	1.1	92.9	2.5	0.4	2.7
Pd/SiO$_2$	1.6	90.2	2.4	0.6	5.1
Ir/NaA	1.3	84.9	9.7	2.1	5.4
Ir/SiO$_2$	2.2	55.2	30.9	6.2	6.5
Rh/NaA	1.2	94.3	1.4	0.4	4.1
Rh/SiO$_2$	1.8	93.5	3.2	0.6	2.5
Ag/NaA	5.2	72.8	22.1	0.5	4.9
Ag/SiO$_2$	1.6	73.4	20.0	0.6	6.1

[a] 4 kPa of methanol, 9 kPa of O_2, 393 K (except 353 K for Pt).
[b] MF: methyl formate. DMM: dimethoxymethane.

Table 4. Selectivities in Isobutanol Oxidative Dehydrogenation[a]

catalyst	conv (%)	product selectivity (%)			
		i-C$_3$H$_7$ CHO	i-C$_3$H$_7$ COOH	i-C$_3$H$_7$COO-i-C$_4$H$_9$	CO_2
Pt/NaA	0.2	86.5	9.3	0.9	3.1
Pt/SiO$_2$	1.4	77.6	18.3	0	2.7
Pd/NaA	1.4	79.8	3.4	2.5	6.7
Pd/SiO$_2$	1.1	76.7	1.9	0.6	5.9
Ir/NaA	0.6	76.5	3.7	4.1	3.7
Ir/SiO$_2$	2.0	88.8	0.7	0.5	5.9
Rh/NaA	0.2	95.2	2.2	0.6	0.7
Rh/SiO$_2$	1.1	92.3	0.4	0.4	5.1
Ag/NaA	0.9	82.3	4.8	3.7	4.5
Ag/SiO$_2$	0.2	95.1	0.7	0.1	2.9

[a] 4 kPa of isobutanol, 9 kPa of O_2, 393 K (except 353 K for Pt).

within NaA than for clusters dispersed within mesoporous SiO$_2$ supports (mean pore diameter: 15 nm), which allow unrestricted access to both large and small reactants. The ratio of these χ values on NaA and SiO$_2$ samples, defined as ϕ, reflects the diffusional constraints in accessing intrazeolite clusters for the larger reactants. A ϕ value of unity is indicative of essentially unconstrained access to metal clusters, as is the case for clusters dispersed within mesoporous SiO$_2$ supports. Larger ϕ values provide strong evidence for preferential containment of active clusters within spatially constrained micropores that can sieve reactants and transition states based on their molecular size and which are inaccessible to the larger reactants.

Alkene hydrogenation led to the exclusive formation of the corresponding alkane on all samples (Table 2), indicating that any residual acid sites did not contribute to the measured chemical reaction rates. Pt/NaA gave much higher turnover rates for ethene than for isobutene (χ_{HD} = 271). These relative rates were much larger than on Pt/SiO$_2$ (χ_{HD} = 2.1), resulting in a ϕ_{HD} value of 130. These data are consistent with the very high specificity for Pt encapsulation during ligand-assisted hydrothermal synthesis. The other metals also gave ϕ_{HD} values much larger than unity (9.8−100; Table 2), reflecting the faster diffusion of ethene relative to isobutene through NaA micropores and the preferential containment of the respective metal clusters within such micropores. Differences in metal cluster size between NaA and SiO$_2$ samples are unlikely to account for these large ϕ_{HD} values because alkene hydrogenation turnover rates depend only weakly on metal cluster size[37,38] and because any such size effects would be similar for ethene and isobutene hydrogenation. Thus, we conclude that active metal surfaces in NaA samples reside preferentially within NaA cages that select ethene (0.39 nm) over isobutene (0.50 nm) with very high specificity. Ethene hydrogenation turnover rates are lower on NaA than on SiO$_2$ samples (by a factor of 0.3−0.6), apparently because access to active cluster surfaces is restricted by diffusion or by limited access to surfaces of clusters tightly contained within NaA cages, even for small ethene molecules.

Alkanol ODH reactions preferentially form selective oxidation products (formaldehyde from methanol and isobutyraldehyde from isobutanol) with low selectivity to combustion products (CO$_2$ < 7%, Tables 3 and 4). Small amounts of condensation products, such as dimethoxymethane (CH$_3$OCH$_2$OCH$_3$, DMM) and isobutyl isobutyrate (i-C$_3$H$_7$COO-i-C$_4$H$_9$), were also detected on metal-containing NaA and SiO$_2$ samples. Selectivities to
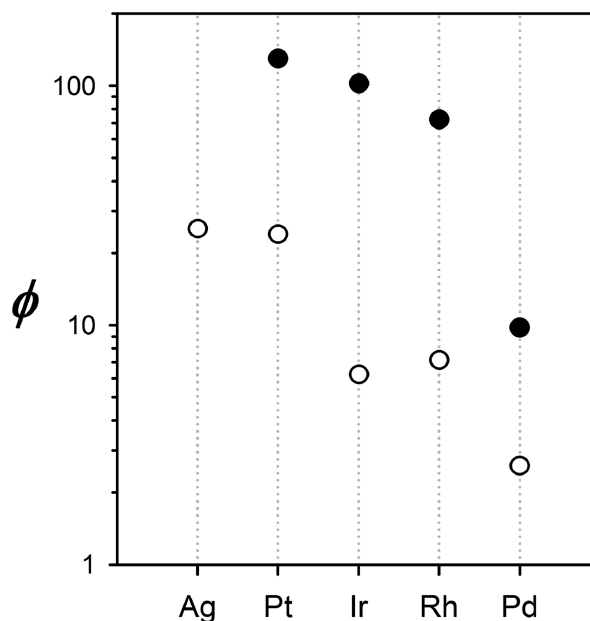

Figure 4. Values of ϕ parameters, reflecting the shape selectivity for various metal/NaA samples, in (▲) alkene hydrogenation (HD), and (○) alkanol oxidative dehydrogenation (ODH). ϕ is defined as the χ value (the ratio of turnover rates for small and large substrates) for M/NaA (M = Ag, Pt, Ir, Rh, and Pd) divided by that for the same metal dispersed on SiO$_2$ for a given reaction; ϕ values larger than unity indicate the preferential containment of clusters within zeolite micropores that can sieve reactants based on size.

formaldehyde and isobutyraldehyde decreased with increasing reactant conversions (varied by changing reactor residence time), as expected from sequential pathways that convert these primary reaction products.[39,40]

As in the case of alkene hydrogenation, alkanol ODH reactions gave ϕ values significantly larger than unity on all samples (ϕ_{ODH} = 2.6−25), but these values were typically smaller than those for alkene hydrogenation (ϕ_{HD} = 9.8−130) (Table 2 and Figure 4). These trends reflect the different diffusivity ratios for ethene−isobutene and methanol−isobutanol reactants within NaA windows and perhaps also a strong dependence of the alkanol ODH reaction on cluster size, which tends to make larger clusters on SiO$_2$ more reactive than smaller clusters encapsulated within NaA.[39] Differences in relative diffusivities are more likely to influence ϕ_{ODH} values than cluster size effects, because the latter are expected to influence methanol

(37) Schlatter, J. C.; Boudart, M. *J. Catal.* **1972**, *24*, 482.
(38) Shaikhutdinov, S.; Heemeier, M.; Baumer, M.; Lear, T.; Lennon, D.; Oldman, R. J.; Jackson, S. D.; Freund, H. J. *J. Catal.* **2001**, *200*, 330.

(39) Lichtenberger, J.; Lee, D.; Iglesia, E. *Phys. Chem. Chem. Phys.* **2007**, *9*, 4902.
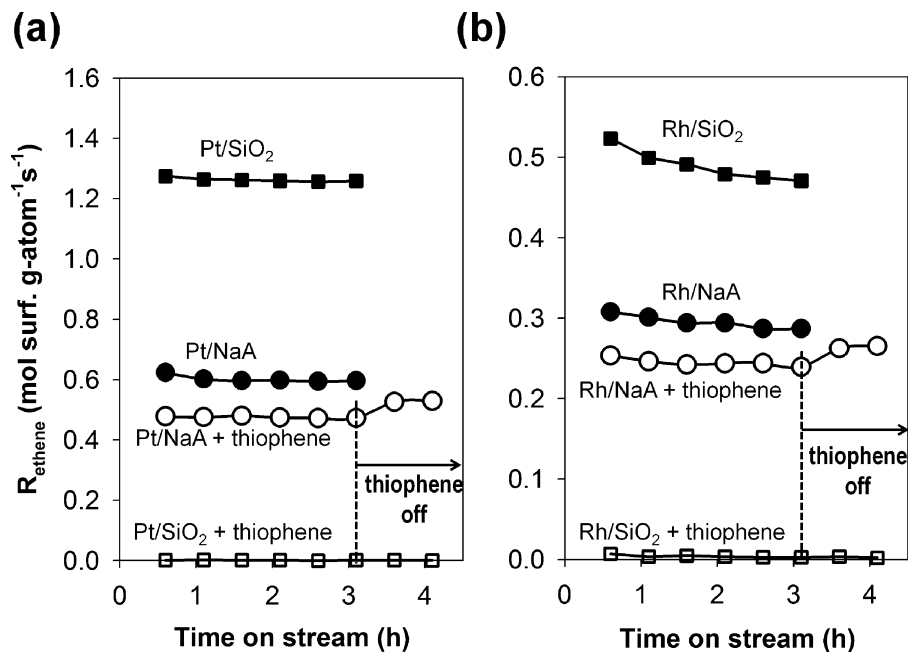(40) Liu, H.; Iglesia, E. *J. Phys. Chem. B* **2005**, *109*, 2155.

Figure 5. Ethene hydrogenation rates for (a) 1.1 wt % of Pt/NaA and 0.79 wt % of PtSiO$_2$ and (b) 1.0 wt % of Rh/NaA and 1.1 wt % of Rh/SiO$_2$ in the presence and absence of thiophene (294 K, 1.5 kPa of ethene, 5 kPa of H$_2$, with/without 0.1 kPa of thiophene).

and isobutanol ODH turnover rates to similar extents, because both require kinetically relevant C−H bond activation on surfaces covered with chemisorbed oxygen, a step disfavored by the larger band gaps of small oxide domains.[40]

The data in Figure 4 demonstrate that both hydrogenation and oxidation probe reactions detect the preferential encapsulation of all metals within NaA using the ligand-assisted synthesis protocols reported here. These data also show the ability of NaA channels to selectively admit smaller reactants to intracrystalline active sites on encapsulated clusters. These spatial constraints also protect metal clusters from larger molecules that can cover their surfaces with strongly bound poisons (e.g., organosulfur compounds) during alkene hydrogenation. Ethene hydrogenation turnover rates were measured on Pt/NaA and Rh/NaA and on their SiO$_2$-supported counterparts with and without thiophene added to the ethene−H$_2$ feed (Figures 5a and 5b). NaA micropore apertures (0.41 nm) are expected to prevent access to encapsulated metal clusters by thiophene (0.46 nm kinetic diameter).[41] The addition of thiophene (0.1 kPa) to ethene−H$_2$ reactants decreased hydrogenation rates by only ∼20% on Pt and Rh clusters in NaA, while SiO$_2$-supported samples showed no detectable hydrogenation rates immediately after thiophene introduction. The small reduction in hydrogenation turnover rate upon thiophene addition for encapsulated clusters appears to partly reflect diffusional constraints imposed by thiophene physisorbed on external surfaces of NaA crystals. Indeed, turnover rates are nearly restored to their initial values upon removal of thiophene from the inlet stream. The small loss of catalytic activity even after the removal of thiophene from the inlet stream can be attributed to the irreversible poisoning of external Pt clusters by thiophene. In contrast, thiophene removal did not restore any detectable hydrogenation activity to unprotected clusters on mesoporous SiO$_2$, indicating that metal surfaces were irreversibly poisoned by thiophene. These data show that encapsulated clusters within small-pore zeolites can be effectively protected against poisoning by organosulfur

compounds, while concurrently demonstrating the high encapsulation selectivity achieved by the synthetic protocols that we report here.

The use of mercaptosilane protecting ligands provide a robust synthetic strategy for the encapsulation of most metals of catalytic interest (e.g., Pt, Pd, Ir, Rh, and Ag) during the hydrothermal crystallization of small-pore zeolites, for which postsynthetic protocols are ineffective, by preventing premature nucleation of metal hydroxides in alkaline media. Encapsulation leads to clusters protected against sintering and contact with toxic impurities within environments that can select reactants and transition states based on molecular size.

Conclusion

We report a general and versatile synthesis protocol for the encapsulation of metal clusters within zeolite micropores using mercaptosilane protecting ligands. This strategy avoids the synchronization of metal hydroxide formation and zeolite crystallization required for unprotected cationic precursors. The mercapto (−SH) group of the silane inhibits the formation of metal hydroxides in the alkaline media required for zeolite synthesis, while the alkoxysilane moiety is hydrolyzed at such conditions and condenses with zeolite precursors to form covalent Si−O−Si or Si−O−Al bonds that induce the crystallization of the inorganic framework around the metal-organosilane complexes. The bifunctional nature of organosilane ligand enables the selective encapsulation of a broad range of metals (Pt, Pd, Ir, Rh, and Ag) within NaA, a zeolite with channel windows too small for postsynthesis encapsulation of metal precursors. The materials exhibited high catalytic shape-selectivities in hydrogenation and oxidative dehydrogenation reactions and remarkable resistance against sulfur poisoning and thermal sintering as a consequence of metal encapsulation in the zeolitic micropores. We expect that the strategy can be extended further to other zeolite and related porous materials having different pore structures and framework compositions by the proper design of protecting ligands. It is reasonable to expect that the present synthetic methods would allow the

(41) Zenga, Y.; Jub, S. *Sep. Purif. Tech.* **2009**, *67*, 71.

encapsulation of not only the reduced metal clusters but also various metal oxides and sulfides by the proper gas treatment (e.g., O_2 and H_2S) after metal encapsulation.

Experimental Section

Material Synthesis. Chemicals including colloidal silica (30 wt %, Aldrich), $NaAlO_2$ (Riedel-de Haën, 53% Al_2O_3, 42.5% Na_2O), NaOH (Aldrich, 99.99%), (3-mercaptopropyl)trimethoxysilane (Aldrich, 95%), H_2PtCl_6 (Aldrich, 99% trace metal basis), $Pd(NH_3)_4Cl_2$ (Aldrich, 99.99%), H_2IrCl_6 (Aldrich, 99.98%), $(NH_4)_3RhCl_6$ (Aldrich, reagent grade), and $AgNO_3$ (Aldrich, 99%) were used as received without further purification.

Metal-encapsulated NaA zeolites were prepared by hydrothermal crystallization in the presence of (3-mercaptopropyl)trimethoxysilane. In a typical synthesis of Pt/NaA, 1.42 g of (3-mercaptopropyl)trimethoxysilane and 9.60 g of NaOH were dissolved in 36.0 g of deionized H_2O ($\sim$0.06 μS cm^{-1} in electrical conductivity). A solution of 0.60 g of H_2PtCl_6 in 36 g of H_2O was added dropwise into the previous solution with vigorous stirring. Colloidal silica (21.3 g) was then added and the mixture was heated to 353 K under stirring until clear Na−silicate solution was obtained. A solution of 12.0 g of $NaAlO_2$ in 36.0 g of H_2O was added to the silicate solution and the solution agitated for 2 h at ambient temperature. The final synthesis gel molar ratios were 1.7 SiO_2/1.00 Al_2O_3/3.2 Na_2O/110 H_2O/0.019 Pt/0.12 (3-mercaptopropyl)trimethoxysilane. The resultant gel was then crystallized hydrothermally at 373 K with stirring for 12 h in polypropylene bottle (Nalgene). The solids formed were isolated by filtration (Pyrex 36060, 10−15 μm fritted funnel) and washed with deionized water until the rinse solution reached a pH of 8. The sample was dried at 393 K for 8 h in ambient air. These procedures were identical for other metal/NaA samples, except for the use of different metal precursors. The (3-mercaptopropyl)trimethoxysilane to metal precursor molar ratio was 6, except for comparison samples in which the ligand was excluded. The removal of the organic moieties was carried out by heating the samples from ambient to 623 at 0.033 K s^{-1} and held for 2 h in flowing dry air (5 cm^3 g^{-1} s^{-1}). After being cooled to ambient temperature, the samples were reduced in flowing H_2 (5 cm^3 g^{-1} s^{-1}) at 623 K (ramping rate: 0.0333 (K s^{-1}) for 2 h. In the case of the Ag/NaA sample, the O_2/H_2 treatments were carried out at 573 K in order to minimize metal sintering during the treatment. Before the exposure to ambient air, all the samples were passivated under flowing 0.5% O_2/He (Praxair, 5 cm^3 g^{-1} s^{-1}) for 1 h at 298 K.

Pt, Pd, Ir, Rh, and Ag clusters supported on mesoporous SiO_2 (Davisil, grade 646, surface area: 294 m^2 g^{-1}, mean pore diameter: 15 nm) were prepared by impregnation to incipient wetness with aqueous solutions of the same metal precursors as used in the NaA encapsulation protocols. The samples were dried at 373 K for 6 h and then treated sequentially in flowing dry air and H_2 following the same procedure used for NaA samples.

Sample Characterization. X-ray diffractograms were measured using a Siemens diffractometer (model D500). Transmission electron micrographs were obtained with a Philips 420 TEM at 120 kV. The samples were embedded into an adhesive polymer, mechanically thinned and dimpled, and further thinned by Ar ion-milling (Gatan 691 Precision Ion Polishing System, 3.0 kV). Particle size distributions were determined by counting at least 200 crystallites. Metal dispersions were determined by chemisorptions of H_2 (99.999%, Praxair) for Pt, Pd, Ir, and Rh and by O_2 (Praxair, 99.999%) for Ag samples using an Autosorb-1 (Quantachrome) analyzer after re-reduction of samples in flowing H_2 for 2 h at 623 K (ramping: 0.083 K s^{-1}) followed by evacuation for 2 h at the same temperature. H_2 adsorption isotherms for Pt, Ir, and Rh samples were measured at 313 K in the pressure range of 10−50 kPa, while H_2 adsorption isotherms for Pd samples were measured at 343 K at 0.4−1.5 kPa to avoid the formation of the β-hydride phase.[42] For O_2 chemisorption on Ag, samples were re-reduced in H_2 for 1 h at 523 K and then evacuated for 2 h at the same temperature. The O_2 adsorption isotherm was measured at 443 K

in the pressure range of 10−30 kPa.[43] Total gas uptake was determined by extrapolation of the high-pressure linear portion of the isotherm to zero pressure. Metal dispersions were calculated by assuming $H/Pt_s = 1$, $H/Pd_s = 1$, $H/Rh_s = 1$, $H/Ir_s = 2$,[44] and $O/Ag_s = 1$[43] stoichiometries.

X-ray absorption spectra were measured at the Stanford Synchrotron Radiation Laboratory using beamline 4−1. Samples (10 mg, 80−120 mesh) were held within a quartz capillary (0.8 mm inner diameter, 0.1 mm wall thickness).[45] The spectra for the Pt/NaA sample were acquired at ambient temperature after re-reduction at 623 K under H_2 flow (5 cm^3 g^{-1} s^{-1}). Three individual spectra were averaged. The pre-edge region was fitted to a second order polynomial curve and postedge background was subtracted using cubic spline routines after spectra were normalized by the absorption edge height. The fine structure region was analyzed using Fourier transform methods and phase shifts and amplitude functions were obtained from FEFF 6. The molecular size of $Pt(S−C_3H_7)_4$ complex was calculated by geometry optimization using molecular mechanics (Polack-Ribiere algorithm, HyperChem 6.03).

Measurements of Reaction Rates and Selectivities. Gases including He (99.999%, Praxair), H_2 (99.999%, Praxair), ethene (99.9%, Praxair), and isobutene (99%, Aldrich) were purified by Agilent O_2/H_2O trap to remove trace amounts of H_2O and O_2. Ethanol (99.99%, Sigama-Aldrich) and isobutanol (99.99%, Sigama-Aldrich) were used as received. Thiophene (99%, Aldrich) was purified over degassed molecular sieve 3A and by repeated freeze−vacuum−thaw cycles by using dry ice/acetone trap (195 K).

Rates and selectivities were measured for hydrogenation of alkenes and oxidative dehydrogenation of alkanols using a packed-bed quartz reactor with plug-flow hydrodynamics. Rates were reported here as turnover rates, defined as the number of molecules converted per time normalized by the number of surface metal atoms determined from chemisorption uptakes. All reaction rates and selectivities were determined at the reactant conversion less than 10%. The catalyst was diluted 10-fold (by mass) using SiO_2 (fumed silica, Cab-O-Sil M5), pressed into a pellet, and sieved to retain 60−80 mesh particles. These diluted catalysts were further mixed with 60−80 mesh quartz granules (treated in concentrated nitric acid and then calcined at 773 K for 4 h in flowing dry air) to avoid temperature gradients caused by the exothermic hydrogenation and oxidative dehydrogenation reactions. Pre-reduced and passivated samples were treated in flowing H_2 (5 cm^3 g^{-1} s^{-1}) at 623 K (573 K for Ag) for 1 h before measuring hydrogenation rates and in 20% O_2/He flow at 393 K for 1 h before oxidation rate measurements. Alkene hydrogenation was carried out using 1.5 kPa of alkene, 5 kPa of H_2, and 93.5 of kPa He as diluent at 294 K (373 K for Ir samples). Alkanol oxidation was carried out using 4 kPa of alkanol, 9 kPa of O_2, and 87 kPa of He as diluent at 393 K (except 353 K for Pt samples). Reactant and product concentrations were analyzed by online gas chromatography (Agilent 6890GC) using a methyl silicone capillary column (HP-1; 50 m × 0.25 mm, 0.25 μm film thickness) and a Porapak Q packed column (80−100 mesh, 1.82 m × 3.18 mm) connected to flame ionization and thermal conductivity detectors, respectively.

(42) Aben, P. C. *J. Catal.* **1968**, *10*, 224.
(43) Hoost, T. E.; Kudla, R. J.; Collins, K. M.; Chattha, M. S. *Appl. Catal., B* **1997**, *13*, 59.

Supporting Information Available: Stabilities of various metal precursors in alkaline solutions, TEM images, and XRD patterns for metal/NaA zeolite and metal/SiO$_2$ samples. This material is available free of charge via the Internet at http://pubs.acs.org.

JA102778E

(44) McVicker, G. B.; Baker, R. T. K.; Garten, R. L.; Kugler, E. L. *J. Catal.* **1980**, *65*, 207.

(45) Lacheen, H. S.; Cordeiro, P. J.; Iglesia, E. *J. Am. Chem. Soc.* **2006**, *128*, 15082.